High Li-ion conductivity in tetragonal LGPO: A comparative first-principles study against known LISICON and LGPS phases

Giuliana Materzanini [1,2,*] Leonid Kahle [1,2,†] Aris Marcolongo [2,3] and Nicola Marzari [1,2]

[1]*Theory and Simulations of Materials (THEOS), École Polytechnique Fédérale de Lausanne, CH-1015 Lausanne, Switzerland*
[2]*National Centre for Computational Design and Discovery of Novel Materials (MARVEL), École Polytechnique Fédérale de Lausanne, CH-1015 Lausanne, Switzerland*
[3]*IBM Research GmbH Zürich, CH-8803 Rüschlikon, Switzerland*

We highlight fast Li-ion diffusion in hypothetical tetragonal $Li_{10}GeP_2O_{12}$ (LGPO), as a counterpart to the well-known phases of orthorhombic (LISICON) LGPO, thio-LISICON, and tetragonal $Li_{10}GeP_2S_{12}$ (LGPS). We use extended Car-Parrinello molecular dynamics in the canonical and isobaric-isothermal ensembles, finding first that tetragonal LGPO is dynamically stable, albeit 0.04 Ha/f.u. above LISICON LGPO. The calculated activation energy for Li-ion diffusion is 0.22 eV, well below the value calculated for LISICON LGPO (0.34 eV), and similar to those for thio-LISICON (0.23 eV) and tetragonal LGPS (0.18 eV). These results indicate that hypothetical tetragonal LGPO, although less stable than its orthorhombic allotrope, shows a room-temperature conductivity comparable to LGPS, and, if synthesized, could make a very attractive Li-ion conductor.

I. INTRODUCTION

A major societal challenge is to limit its reliance on fossil fuels by switching to renewable and green energy sources [1], a goal that cannot be achieved unless an efficient way to store electrical energy is provided [2]. Electrochemical storage is particularly suited to meet the needs of electrical grids powered by sun, wind, or tides [3,4], and it can also enable the electrification of transportation, providing the energy to automotive vehicles that are less dependent on fossil fuels—hybrid electrical, hybrid plug-in electrical, and pure electrical vehicles [5]—as well as the electrification of residential services, as exemplified by the Tesla Home Battery Powerwall [6].

Among the existing electrochemical technologies, Li-ion batteries, about 30 years after their first commercial introduction by Sony in 1991 [7–9], offer some of the best performance in terms of energy density, memory effects, near-reversibility, and longer life cycles [10,11], and they have enabled the rise of portable electronics and furnished the power supply for safety systems, personal transportation, and digital technologies [12]. Smart-grid integration and mass-market full electrification are the next frontiers, and for that reason the complex tradeoff between energy density (and thus range), power density, cost, and safety of batteries needs to be addressed [13,14], in addition to the availability of the raw materials [15]. A Li-ion battery cell exploits the redox activities of the anode and cathode to generate electricity outside the cell while reversibly intercalating Li ions between the two electrodes through an ionic conducting electrolyte [11].

Due to dendrite formation and explosive failure with Li metal anodes [9,16,17], the anode, like the cathode, is an insertion material [18,19], and nonaqueous electrolytes are usually exploited due to their wider electrochemical windows compared to water-based electrolytes ($\sim$4.2 V versus $\sim$1.2 V [20,21]). Energy density has been considered the preeminent figure-of-merit to date in Li-ion batteries, and huge efforts have been put into the design of cathodes with high voltages and capacities [22,23], focusing on three main classes of cathodes, based, respectively, on the $LiCoO_2$ intercalation structure [24], the $LiMn_2O_4$ spinel structure [25], and the polyanion olivine structure [26]. For example, by partially substituting the Co cations with Ni, Mn, or Al in $LiCoO_2$ and successively increasing the Li concentration in the material, the capacity of $LiCoO_2$ was almost doubled [19,27,28], and partially replacing the Mn^{3+}/Mn^{4+} couple with Ni^{2+}/Ni^{4+}, Cr^{3+}/Cr^{4+}, Fe^{3+}/Fe^{4+}, and Co^{3+}/Co^{4+} in $LiMn_2O_4$ has given rise to new generations of high-voltage (5 V) cathodes [25,29]. However, the effort to design high-energy cathodes cannot come without a parallel effort to address the safety and efficiency challenges that arise when the interaction between the current electrolytes and the electrodes is taken into account. Examples include the combustion reactions of high-capacity cathodes ($Li_{0.5}CoO_2$ and its derivatives) in the presence of ethylene or propylene carbonate electrolytes at temperatures above 180 °C [28,30], the Mn dissolution of $LiMn_2O_4$ in the electrolyte with subsequent oxidation and degradation of the electrolyte and capacity loss of the cell [31], and in general the oxidations (reductions) of the electrolyte if the electrochemical potentials of the cathode (anode) are outside the electrolyte stability window [11]. Although the latter issue is spontaneously fixed by the formation of the solid electrolyte interface (SEI) that widens the electrochemical window of the electrolyte [21], this interface is usually also responsible for the low ionic transport from the electrolyte to the electrode and *vice versa*.

*Author to whom all correspondence should be addressed: giuliana.materzanini@epfl.ch
†Present address: IBM Research GmbH Zürich, CH-8803 Rüschlikon, Switzerland.

Usually, electrolyte decomposition occurring at more than 4.2 V versus Li$^+$/Li is considered the main reason for the capacity fading upon cycling [32]. Finally, when the passivating interface is destroyed at high temperatures (even 80 °C), liquid organic electrolytes in contact with the positive material can form highly toxic fluoro-organic compounds [33]. All these issues make the use of state-of-the-art Li-ion batteries for electromotive applications (where the considerable size and weight of the batteries make these much more exposed to a fire risk during short circuits) a technology still in need of safety and performance improvements, to the extent that its original scope, i.e., addressing some core environmental problems, is still a matter of debate [13].

Some safety challenges can in principle be addressed through an all-solid-state battery strategy by substituting liquid organic with solid-state (crystalline, glassy, or amorphous) inorganic electrolytes [34–43]. In addition to solving several safety issues and the problem of leakage presented by the currently used organic electrolytes, these materials have a lithium transport number very close to 1 [36], better thermal stability, and wider electrochemical windows, and they can enable the use of Li metal anodes [41,44]. Historically, the drawbacks have been a generally lower ionic conductivity with respect to organic electrolytes, and the need for a complex engineering of the electrolyte/electrode interface [17]. In this respect, sulfides proved to be an interesting choice, presenting a superior ionic conductivity with respect to many other materials. Moreover, their softness reduces grain boundary resistance and facilitates the manufacture of electrode/electrolyte interface [45,46]. The LISICON (LIthium SuperIonic CONductors) family of superionics, thoroughly investigated in the 1960s, 1970s, and 1980s [47–54], was originally composed of oxide materials, solid solutions between hcp-based γ-Li$_3$PO$_4$-structure crystals (wurtzite-based edge-sharing tetrahedra with cations at the center and anions at the corners [55–58]), and tetragonal close-packed Li$_4$YO$_4$ crystals (with $Y =$ Ge,Si,Ti) [59–62]. Through x-ray and neutron diffraction techniques, the structures were determined to be monoclinic [61] or orthorhombic, both in the solid solutions and in the parent phases [56,58,63]. Forming solid solutions such as Li$_{(3+x)}$Y$_x$P$_{(1-x)}$O$_4$ or Li$_{(2+2x)}$Zn$_{(1-x)}$GeO$_4$, i.e., tuning stoichiometries such as Li$_3$PO$_4$ [56] or Li$_2$ZnGeO$_4$ (where the number of cations and anions is the same) [50] toward stoichiometries such as Li$_4$YO$_4$ [64], introduces Li interstitials in the pristine wurtzite structure [50,56] and favors ionic conductivity [48], which usually reaches a maximum at intermediate values of x in the solid solutions (see, e.g., [51]). However, it became clear that replacing oxygen with sulfur, with a larger ionic radius and a more polarizable character [65], could improve the conductivity. The thio-LISICON Li$_{(4-x)}$P$_x$Ge$_{(1-x)}$S$_4$ family [66], a solid solution between the parent phases Li$_3$PS$_4$ [67–69] and Li$_4$GeS$_4$ [70], was studied for glass, glass-ceramic [71–75], and crystalline systems [66,76,77], showing superior conductivity with respect to the oxides, with the best conductivity at room temperature (2×10^{-3} S cm^{-1}) reached for $x = 0.75$ [66]. In an additional effort to improve conductivity, a new phase (tetragonal, space group $P4_2/nmc$, no. 137) at the composition $x = 0.67$, i.e., Li$_{10}$GeP$_2$S$_{12}$ (LGPS), was discovered in 2011 [78], with a record conductivity of 1.2×10^{-2} S cm^{-1} and a structural arrangement significantly different from the thio-LISICON phases [79]. This inspired a new wave of efforts, both experimental [80–93] and theoretical [79,94–101], aiming to understand conduction mechanisms and to push the ionic conductivity even further. By tuning lithium, germanium, and phosphorus compositions, a room-temperature conductivity of 1.4×10^{-2} S cm^{-1} was reached [90], and by substituting germanium with silicon and simultaneously partially replacing sulfur with chlorine, a value of 2.5×10^{-2} S cm^{-1} was obtained [92]. For an extensive up-to-date overview of LGPS and LGPS-like materials, we refer the reader to the recent review by Kanno and co-workers [102].

However, apart from the high ionic conductivity that places these sulfide conductors at the same level of liquid ionic electrolytes, there are important drawbacks that cannot be disregarded when trying to deploy them as electrolytes for all-solid-state batteries. First of all, LGPS and LGPS-like sulfides have very narrow thermodynamical electrochemical stability windows. Results from simulations [94,98] and impedance spectroscopy [103,104] show that LGPS is chemically unstable below 1.71 V versus Li$^+$/Li as a consequence of Ge and P cation reduction at Li metal [104] or Li alloy [103] anodes, yielding lithiation products Li$_{15}$Ge$_4$, Li$_3$P, and Li$_2$S; it is also unstable above 2.14 V due to the sulfur oxidation at the cathode, with delithiation products P$_2$S$_5$, GeS$_2$, and S [105]. Both calculations and experiments agreed on the electrochemical stability of LGPS and pointed out its claimed wide (5 V) electrochemical window [78] as being essentially kinetic [98,104]. Although this interfacial instability can in principle be dealt with by using coating oxide layers [100], the solid electrolyte interface, mainly formed due to the chemical instability at the anode of Ge in the LGPS tetragonal structure [103], shows high resistance (4.6 Ω cm^2 after one year [104]), and the requirement for high Li-ion conductivity across the interface remains a key challenge to be addressed [106]. In principle, neither a Li metal anode nor high-voltage cathodes (both targeting improved energy density) can be used with LGPS unless coatings are exploited, as is the case for the liquid electrolytes. Moreover, sulfides show a well-known hygroscopicity as well as instability in air in the potential range of normal Li battery operation [45,75,107,108], they can provoke corrosion of the vacuum chamber [109], and a careful suppression of hydrolysis is mandatory in order to stop these materials from decomposing and generating harmful (and lethal) H$_2$S. All these issues would suggest the need to turn to a safer electrolyte that does not require the engineering of a coating film protecting the electrodes (which is also the case for liquid electrolytes), while evaluating if this would hamper ionic conductivity. Safety, nontoxicity, and no hazard risks are also the main reasons justifying the interest in solid-state electrolytes, and when seeking improved material performance one should not forget the original goal of large-scale electrochemical storage, i.e., establishing a nontoxic and sustainable-energy economy. For the above reasons, oxygen-substituted Li$_3$PS$_4$ [110–114] and LGPS-like [115–117] superionic conductors, and in general oxysulfides [118], as well as non-sulfur-substituted LISICON materials [119,120], have recently been considered in the literature.

Oxides are expected to be more electrochemically stable on the cathode side (for example, the cathode coating for LGPS should be in principle an oxide [100,106]), and the chemical stability of LGPS at the anode side is expected to improve by substituting sulfur with oxygen, which creates stronger covalent Ge-O bonds [115]. Chlorine-substituted Ge- and Si-based LISICONs show large electrochemical windows up to 9 V [121], and oxygen-substituted Li_3PS_4 with the same structure of tetragonal LGPS shows a wide electrochemical window of 5 V [110], as predicted by simulations for oxygen-substituted tetragonal LGPS [96]. In addition, partially-oxygen-substituted tetragonal LGPS shows room-temperature conductivity only slightly inferior to LGPS, and almost the same activation energy [115]. The latter result is at variance with calculations that for the oxide analog of tetragonal LGPS, $Li_{10}GeP_2O_{12}$ (LGPO), predict almost twice the activation barrier as for LGPS [96]. So far, there is no experimental evidence for this phase of LGPO, but only for a LISICON material obtained as a solid solution of γ-Li_3PO_4 and Li_4GeO_4 [51] and having the same composition as LGPO, i.e., $Li_{(4-x)}Ge_{(1-x)}P_xO_4$ with $x = 0.67$, whose structure, reported in Ref. [122], belongs to the same space group as γ-Li_3PO_4 (*Pnma*, no. 62) and for which the moderate ionic conductivity of 1.8×10^{-6} S cm^{-1} at $40\,^{\circ}$C is reported in Ref. [123] (see also Refs. [119,120]). Thus, an in-depth investigation of the structure and conductivity of the oxygen-substituted tetragonal LGPS and of the experimentally reported orthorhombic phase of LGPO becomes important to investigate the feasibility of oxygen substitution to solve the above safety and instability problems of LGPS. In addition, whereas many simulations exist for the tetragonal phase of LGPS [79,94,96,124], so far there have been no theoretical studies on the less conductive, monoclinic (quasi-orthorhombic) thio-LISICON phases [66]. Comparing oxides and sulfides in different phases would also be important in order to relate structure and anionic substitution to conductivity in these superionics.

In this paper, we address with first-principles molecular dynamics simulations Li-ion diffusion in a hypothetical tetragonal phase of LGPO, chosen to have the same structure as tetragonal LGPS [78] (space group $P4_2/nmc$, no. 137). Diffusion coefficients are extracted from long ($\sim$160 ps) trajectories, generated within the NVE and NVT ensembles. Furthermore, the phase stability of hypothetical tetragonal LGPO is investigated by means of NPT simulations, and its electrochemical stability explored by evaluating the band gap from density-of-states (DOS) calculations. To get a useful comparison, we provide the same investigations for the genuine LISICON orthorhombic phase of LGPO (space group *Pnma*, no. 62 [122]), for the tetragonal phase of LGPS [78,81], and for an orthorhombic structure for LGPS adopted from orthorhombic LGPO [122], which should be a good approximation to the monoclinic thio-LISICON II phase [66] (see Sec. II A). It is worthwhile to clarify here that, in analogy with the use, in the literature, of the term "thio-LISICON" to indicate both a family of superionic conductors [66] and the monoclinic (quasi-orthorhombic) phases of LGPS [66,79], throughout this paper the term "LISICON" indicates both a family of superionic conductors [47–54] and the known

orthorhombic phase of LGPO [122]. Just as for LGPS the thio-LISICON phases (monoclinic) are contrasted with the tetragonal LGPS phase throughout the literature [79], here for LGPO we contrast the LISICON phase (orthorhombic) with the (hypothetical) tetragonal LGPO phase. In the remainder of this paper, we will refer to hypothetical tetragonal $Li_{10}GeP_2O_{12}$ as t-LGPO, to orthorhombic $Li_{10}GeP_2O_{12}$ [122] as o-LGPO, to tetragonal $Li_{10}GeP_2S_{12}$ [78,80] as t-LGPS, and to the above-described orthorhombic $Li_{10}GeP_2S_{12}$ as o-LGPS.

The paper is organized as follows. In Sec. II we describe the methods employed, from the supercell construction to the first-principles simulations and the extraction of the diffusion coefficients from the simulations. Results for diffusion, phase stability, and band gaps are presented in Secs. III, IV, and V, respectively. A general discussion and the conclusions follow in Secs. VI and VII, respectively.

II. METHODS

A. Supercell construction

For t-LGPO we use the same 50-atom supercell already used in previous studies for t-LGPS [96,124], starting from the crystallographic positions for the tetragonal cell ($P4_2/nmc$) of t-LGPS [78,81] [Fig. 1(a)] and adapting its volume to LGPO, as explained below. For o-LGPO we build a 100-atom ($1 \times 1 \times 3$) supercell from the unitary cell (orthorhombic *Pnma*) reported in Ref. [122] for orthorhombic LGPO [Fig. 1(b)]. For t-LGPS we use the above-mentioned 50-atom supercell [96,124]. For o-LGPS we adapt the above-described o-LGPO 100-atom supercell to the volume of a ($1 \times 1 \times 3$) supercell of type II thio-LISICON $Li_{(4-x)}Ge_{(1-x)}P_xS_4$ at $x = 0.65$ (Table I in Ref. [66]). The latter choice is due to the fact that the space group and atomic positions of the thio-LISICON phases I, II, and III in Ref. [66] are not available, as also noted in Ref. [79], so that we could not simulate the genuine monoclinic thio-LISICON phase II of Ref. [66], but only an orthorhombic approximation to it, that we provide based on Ref. [122] for LGPO. We exploit the volume ratio between the LISICON [122] and thio-LISICON [66] structures to determine the t-LGPO volume from the experimental t-LGPS volume [78,81].

After relaxing the atomic positions and lattice vectors with the Broyden-Fletcher-Goldfarb-Shanno algorithm, as described in Sec. S I of the Supplemental Material (Ref. [125] and references therein), we use these configurations (with a small randomization added for the atomic positions) to start the molecular dynamics simulations presented below. The relaxed structures—atomic positions and unit cells—are also published on the Materials Cloud Archive [126].

B. Car-Parrinello molecular dynamics

We use Car-Parrinello (CP) molecular dynamics [127], based on Kohn-Sham density-functional theory (DFT) [128,129] in the plane-wave pseudopotential formalism [130,131], as implemented in the cp code of the QUANTUM ESPRESSO distribution [132].

Instead of solving self-consistently the Kohn-Sham equations at each MD step and following a trajectory on the Kohn-Sham Born-Oppenheimer (BO) energy surface $E^{KS}[\mathbf{R}]$ [129], in CP one follows a trajectory on the fictitious energy

(a) t-LGPO 50-atom supercell.
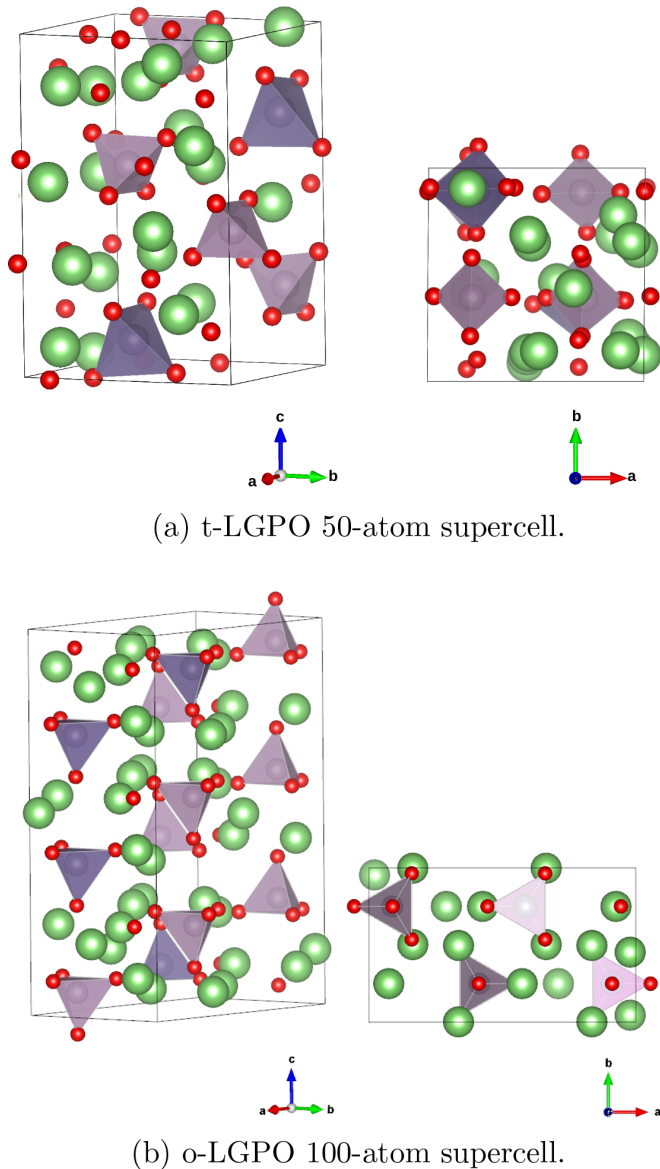

(b) o-LGPO 100-atom supercell.

FIG. 1. The 50- and 100-atom supercells (left: 3D view, right: top view) used in the simulations for (a) t-LGPO and (b) o-LGPO from Refs. [78] and [122], respectively (see the text). Li atoms are displayed in green, O atoms are in red, and Ge and P atoms are at the center of the dark and light purple tetrahedra, respectively. The analogous LGPS supercells (see the text) have sulfur atoms replacing oxygen atoms. Images generated by using VESTA [180].

surface of the coupled electron-ion Lagrangian, which is a functional of both ionic degrees of freedom and electronic wave functions [127]:

$$
\mathcal{L}^{\mathrm{CP}} = T_{\mathrm{ions}} + T_{\mathrm{el}}^{\mathrm{fict}} - E^{\mathrm{CP}}[\{\psi_j\}, \mathbf{R}]
$$
$$
- \sum_{jk} \Lambda_{jk} \left(\int d\mathbf{r} \, \psi_j(\mathbf{r}) \psi_k(\mathbf{r}) - \delta_{jk} \right). \quad (1)
$$

Compared to the Lagrangian of the physical system, the Car-Parrinello Lagrangian [reported in Eq. (1) for the *NVE* case] contains $E^{\mathrm{CP}}[\{\psi_j\}, \mathbf{R}]$ in place of $E^{\mathrm{KS}}[\mathbf{R}]$ (i.e., the "instantaneous" Kohn-Sham energy for wave functions ψ_j not

necessarily on the Born-Oppenheimer surface), the Lagrange multipliers $\{\Lambda_{jk}\}$ to ensure orthonormality of the electronic wave functions, and the fictitious kinetic energy $T_{\mathrm{el}}^{\mathrm{fict}}$ of the electronic wave functions

$$
T_{\mathrm{el}}^{\mathrm{fict}} = \mu \sum_i \int |\dot{\psi}_i|^2 d\mathbf{r}, \quad (2)
$$

that has no relation to the physical quantum kinetic energy of the electrons [133], but allows for a dynamical evolution of the Kohn-Sham states following the ionic motion. The parameter μ, whose dimensionality is $[m \times l^2]$ or $[E \times t^2]$, needs to be chosen sufficiently small in order to ensure that $T_{\mathrm{el}}^{\mathrm{fict}}$ is small compared to the kinetic energy of the ions $T_{\mathrm{ions}} = \sum_i^{N_{\mathrm{ions}}} \frac{1}{2} m_i \mathbf{v}_i^2$, so as to avoid an irreversible transfer of energy from the "hot" ions to the fictitious degrees of freedom, which would gain kinetic energy and move away from the Kohn-Sham surface during the dynamics [131,134]. However, a smaller μ implies a smaller time step in the integration of the equations of motion, to ensure accuracy and to keep numerically correct the constant of motion during the dynamics. In the Supplemental Material [125] (Sec. S II and references therein), we report these quantities for the *NVE* simulations of t-LGPO, and we show that the choice of $\mu = 500$ a.u. and time step $dt = 4$ a.u. satisfies the criteria discussed above. A similar analysis for t-LGPS is reported in the supplemental material of Ref. [124], resulting in the same values for μ and dt. In analogy with Ref. [124] for t-LGPS, we employ for t-LGPO norm-conserving pseudopotentials [135,136] with a plane-wave cutoff $E_{\mathrm{cut}} = 80$ Ry. Thanks to the release of version 1.1 of the SSSP library [137,138], we chose a lower cutoff $E_{\mathrm{cut}} = 50$ Ry and ultrasoft pseudopotentials (with a 400 Ry cutoff for the electron density) [139] using the Standard Solid State Pseudopotential (SSSP) Efficiency library 1.0 [137] (GBRV [139] for Li, O, and S; PSLib [140] for Ge and P) for o-LGPS and o-LGPO. Brillouin zone integrations are performed using the Γ point, and the exchange-correlation functional is PBE [141].

To perform *NVT* simulations (Sec. III), the Lagrangian of Eq. (1) is modified by adding a kinetic term and a potential energy term, which take into account the presence of a chain of Nose-Hoover [142] thermostats of temperature T [143]. Tuning the frequency of the thermostat chain is explained in the Supplemental Material [125] (Sec. S III and references therein), together with a comparison of *NVE*- and *NVT*-calculated Li-ion diffusion coefficients in t-LGPO, to evaluate the effect of the thermostat on the final results. For the *NPT* simulations (Sec. IV), the Lagrangian of Eq. (1) is modified by adding both kinetic and potential energy terms of a Nose-Hoover thermostat chain [142,143] and of a Parrinello-Rahman barostat [144,145].

C. Extraction of the tracer diffusion coefficients

The mean-square displacement of a given ionic species is a measure of its mobility in a material, and it can be put in direct relationship with the self-diffusion coefficient. The latter is also known (and will be referred to from now on) as the tracer diffusion (D_{tr}) coefficient, as it can be compared to pulsed-field gradient nuclear magnetic resonance experiments [146]. According to the Einstein relation for diffusion [147–149], the

tracer diffusion coefficient in three dimensions is

$$D_{\text{tr}}^{\text{Li}} = \lim_{t \to \infty} \frac{1}{6} \frac{d}{dt} \text{MSD}_{\text{tr}}^{\text{Li}}(t), \tag{3}$$

where the Li-ion tracer mean-square displacement $\text{MSD}_{\text{tr}}^{\text{Li}}(t)$ in a system of N_{Li} ions over a sufficiently long time t (no ballistic regime) is [148]

$$\text{MSD}_{\text{tr}}^{\text{Li}}(t) = \frac{1}{N_{\text{Li}}} \sum_{i}^{N_{\text{Li}}} \langle |\mathbf{R}_i(t' + t)] - \mathbf{R}_i(t')|^2 \rangle, \tag{4}$$

with $\mathbf{R}_i$ being the instantaneous position of the ith Li ion, and $\langle \cdots \rangle$ denoting an average over the times t'. For the method employed to calculate $\text{MSD}_{\text{tr}}^{\text{Li}}(t)$, $D_{\text{tr}}^{\text{Li}}$, and their statistical uncertainties [149–151] from the molecular dynamics simulations, we refer the reader to the Supplemental Material [125] (Sec. S IV and references therein).

Furthermore, from the tracer coefficient $D_{\text{tr}}^{\text{Li}}$ the ionic conductivity σ (entirely ascribed to the Li ions) can be calculated according to the Nernst-Einstein equation:

$$\sigma(T) = \frac{N_{\text{Li}} Z_{\text{Li}}^2 e^2}{V k_B T} D_{\text{tr}}^{\text{Li}} = \frac{N_{\text{Li}} e^2}{V k_B T} D_{\text{tr}}^{\text{Li}}. \tag{5}$$

In Eq. (5), N_{Li}/V is the density of the charge carriers (i.e., the Li ions), $Z_{\text{Li}} e = e$ is their charge (e being the elementary charge and assuming that the average Born effective charge is $+1$, see also Ref. [152]), and $D_{\text{tr}}^{\text{Li}}$ is the self-diffusion coefficient from Eq. (3). From Eq. (5), assuming a negligible change of volume with temperature, the temperature dependence for $D_{\text{tr}}^{\text{Li}}$ is the same as for σT.

D. Extraction of the collective diffusion coefficients

As pointed out in Refs. [124,153,154], the tracer diffusion coefficient of Eq. (3) assumes independent uncorrelated contributions from all the ions. The so-called charge diffusion coefficient D_σ [155,156] provides a more realistic estimate, as it accounts for ion-ion correlated diffusion. For a Li ion in a system of N_{Li} ions, it can be written [155,156]

$$D_\sigma^{\text{Li}} = \lim_{t \to \infty} \frac{\text{MSD}_\sigma^{\text{Li}}(t)}{6t}, \tag{6}$$

where

$$\text{MSD}_\sigma^{\text{Li}}(t) = \frac{1}{N_{\text{Li}}} \sum_{i,j}^{N_{\text{Li}}} \langle [\mathbf{R}_i(t'+t) - \mathbf{R}_i(t')][\mathbf{R}_j(t'+t) - \mathbf{R}_j(t')] \rangle \tag{7}$$

so that the corrected Nernst-Einstein equation [124] includes the collective $\text{MSD}_\sigma^{\text{Li}}(t)$ [Eq. (7)] through D_σ^{Li} [Eq. (6)]:

$$\sigma(T) = \frac{N_{\text{Li}} e^2}{V k_B T} D_\sigma^{\text{Li}}. \tag{8}$$

It is worthwhile to mention that $D_{\text{tr}}^{\text{Li}}$ and D_σ^{Li} have been derived here in the Einstein formalism (i.e., from the mean-square displacement), whereas in Ref. [124] the same quantities are reported in the Green-Kubo formalism [157].

III. Li-ION DIFFUSION IN t-LGPO

A. Tracer diffusion

From the t-LGPO NVT CP simulations, we calculate $\text{MSD}_{\text{tr}}^{\text{Li}}(t)$ [Eq. (4)] and $D_{\text{tr}}^{\text{Li}}$ [Eq. (3)] of t-LGPO at all temperatures considered. The same calculations are also performed, for reference, from the NVT CP dynamics of o-LGPO, t-LGPS, and o-LGPS. The details of these simulations are reported in the Supplemental Material [125] (Sec. S V and references therein). In Fig. 2(a) we report $\text{MSD}_{\text{tr}}^{\text{Li}}(t)$ and the corresponding $D_{\text{tr}}^{\text{Li}}$ for t-LGPO, at the representative temperature of 900 K. $\text{MSD}_{\text{tr}}^{\text{Li}}(t)$ and $D_{\text{tr}}^{\text{Li}}$ at 900 K for o-LGPO, t-LGPS, and o-LGPS are reported in Figs. 2(b), 2(c) and 2(d), respectively. At this temperature, we note that diffusion is equally fast, approximately, in t-LGPO as in t-LGPS and in o-LGPS, while being much slower in o-LGPO. Results for the other temperatures (not shown here) display a similar trend.

We consider diffusion here as an activated process that obeys an Arrhenius law [158]:

$$\ln D_{\text{tr}}^{\text{Li}}(T) = \ln A - \frac{E_{a_{D_{\text{tr}}^{\text{Li}}}}}{k_B T}, \tag{9}$$

where the constant A is related to the attempt frequency, whereas the activation energy $E_{a_{D_{\text{tr}}^{\text{Li}}}}$ is the energy barrier for the diffusion. We report the Arrhenius plot for $D_{\text{tr}}^{\text{Li}}$, in the widely used form $\log_{10} D_{\text{tr}}^{\text{Li}}(1000/T)$, in Fig. 3. As observed in Fig. 2 for diffusion at one temperature, also the temperature dependence of the diffusion coefficients (Fig. 3) reveals basically two different cases: highly diffusive systems (t-LGPO and the two sulfide phases), and a less diffusive one (o-LGPO). This finding, while being in qualitative agreement with existing experimental literature that reports a rather high activation barrier ($\sim$0.54 eV) for o-LGPO [120,123], and low activation barriers ($\sim$0.25 eV) for t-LGPS [78] and o-LGPS [66], adds an interesting piece of information on the hypothetical t-LGPO, which is predicted to have a low activation barrier and high diffusion.

B. Collective diffusion

In Fig. 4(a) we report the Arrhenius plot for Li-ion charge diffusion [Eq. (6), blue line], compared to the tracer diffusion [Eq. (3), red line], in t-LGPO. The same is displayed in Figs. 4(b), 4(c) and 4(d) for the comparative phases o-LGPO, t-LGPS, and o-LGPS, respectively. In Table I, the activation energies for diffusion from $D_{\text{tr}}^{\text{Li}}$ [Eq. (9)] and D_σ^{Li} [the latter obtained from Eq. (9) by substituting D_σ^{Li} to $D_{\text{tr}}^{\text{Li}}$] are reported for t-LGPO and for the other phases, together with available experimental results for σT [66,80,120] and with results from first-principles calculations in the literature for t-LGPO and t-LGPS [96]. As already noted in Ref. [124] for t-LGPS, also for t-LGPO, o-LGPO, and o-LGPS the activation energy remains approximately unchanged when including ion-ion correlations, i.e., comparing $E_{a_{D_{\text{tr}}^{\text{Li}}}}$ with $E_{a_{D_\sigma^{\text{Li}}}}$ (Fig. 4 and Table I). We also note that the statistical errors for D_σ^{Li} are systematically higher than for $D_{\text{tr}}^{\text{Li}}$, due to the well-known slower convergence of the former in the time averages [124]. Figure 4 and Table I confirm that o-LGPO has moderate conducting properties, in qualitative agreement with experiments [123], that place
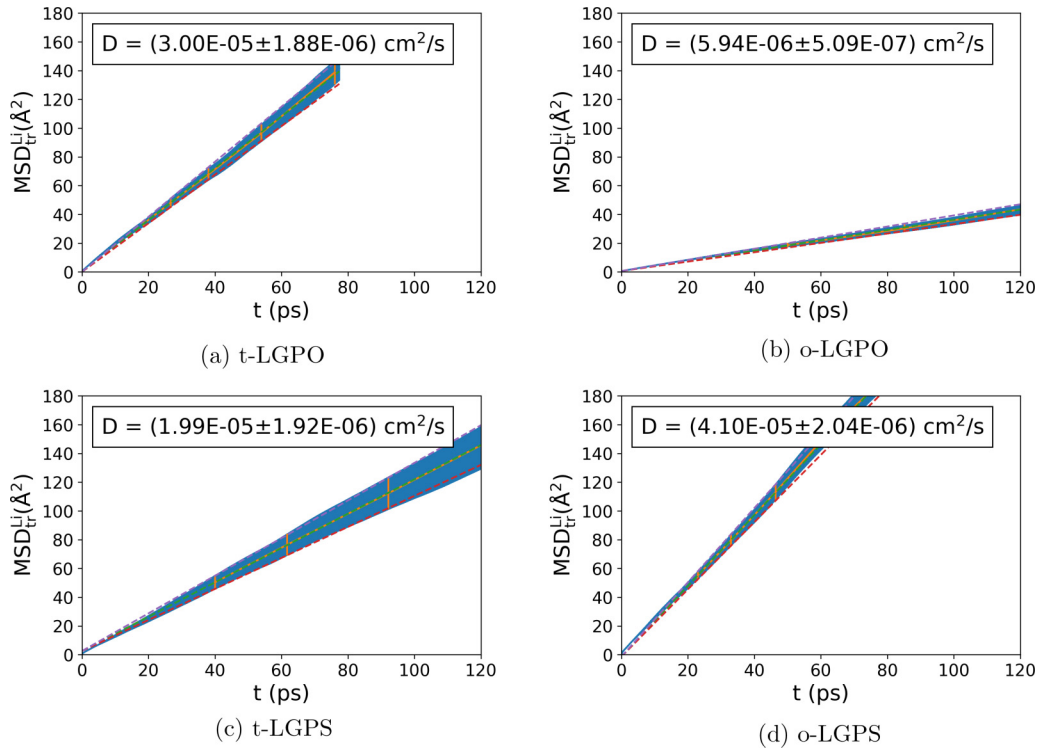
FIG. 2. Li-ion tracer mean-square displacement $\mathrm{MSD}_{\mathrm{tr}}^{\mathrm{Li}}(t)$ [Eq. (4)] for t-LGPO (a), compared with o-LGPO (b), t-LGPS (c), and o-LGPS (d), from 900 K-NVT CP (a,b,d) and NVE CP (after 900 K-NVT CP [124]) (c) simulations. For each system, a maximum elapsed time t is set for the calculation of $\mathrm{MSD}_{\mathrm{tr}}^{\mathrm{Li}}(t)$, and the rest of the trajectory is used to perform the statistical average $\langle \cdots \rangle$ in Eq. (4), so that the time ranges displayed in the plots are shorter than the total times of the simulations (see the Supplemental Material [125], Sec. S IV). In each plot, the green dashed curve represents the value of $\mathrm{MSD}_{\mathrm{tr}}^{\mathrm{Li}}(t)$ from Eq. (4), and the orange points and errorbars, giving rise to the continuous blue cone and to the lower and upper limits of $\mathrm{MSD}_{\mathrm{tr}}^{\mathrm{Li}}(t)$ (red curves), are the uncorrelated $\mathrm{MSD}_{\mathrm{tr}}^{\mathrm{Li}}(t)$ and errors from the block analysis described in the Supplemental Material [125] (Sec. S IV).

this material among the candidate solid electrolytes for microbatteries [120]. The diffusivity of hypothetical tetragonal LGPO, however, is some orders of magnitude superior to
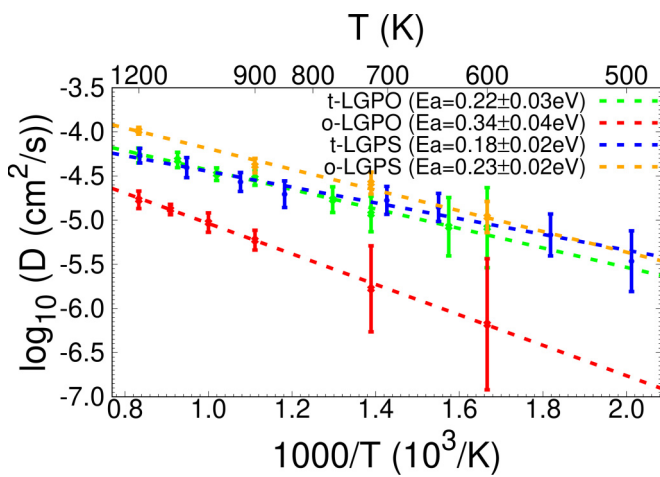
its orthorhombic allotrope [122,123] at all temperatures, and comparable to its more studied sulfide analog [78,80]. This finding, which is at variance with previous first-principles results [96], but in agreement with a recent computational study exploiting an *ab initio* trained frozen-lattice potential [159], could hopefully pave the way to experimental attempts aimed at synthesizing LGPO in the same structure as tetragonal LGPS [115].

FIG. 3. Arrhenius plot and corresponding activation energy for Li-ion tracer diffusion coefficient $D_{\mathrm{tr}}^{\mathrm{Li}}$ [Eq. (3)] in t-LGPO from NVT CP molecular dynamics (cf. Fig. 2), compared with o-LGPO, t-LGPS, and o-LGPO, in the range of temperatures studied. Errors are calculated from the block analysis described in the Supplemental Material [125] (Sec. S IV).

TABLE I. Activation energies in eV [Eq. (9)] for t-LGPO Li-ion tracer diffusion [Eq. (3) and Fig. 3] and charge diffusion [Eq. (6) and Fig. 4] (first line), compared with o-LGPO, t-LGPS, and o-LGPS (following lines). We compare with results of a previous *ab initio* investigation on Li-ion diffusivity in t-LGPO and t-LGPS [96], and with activation energies for σT (conductivity times temperature) from the experimental literature [66,80,120] [note that, from Eq. (5), the diffusion coefficient and σT have the same temperature dependence, and thus the same activation energy].

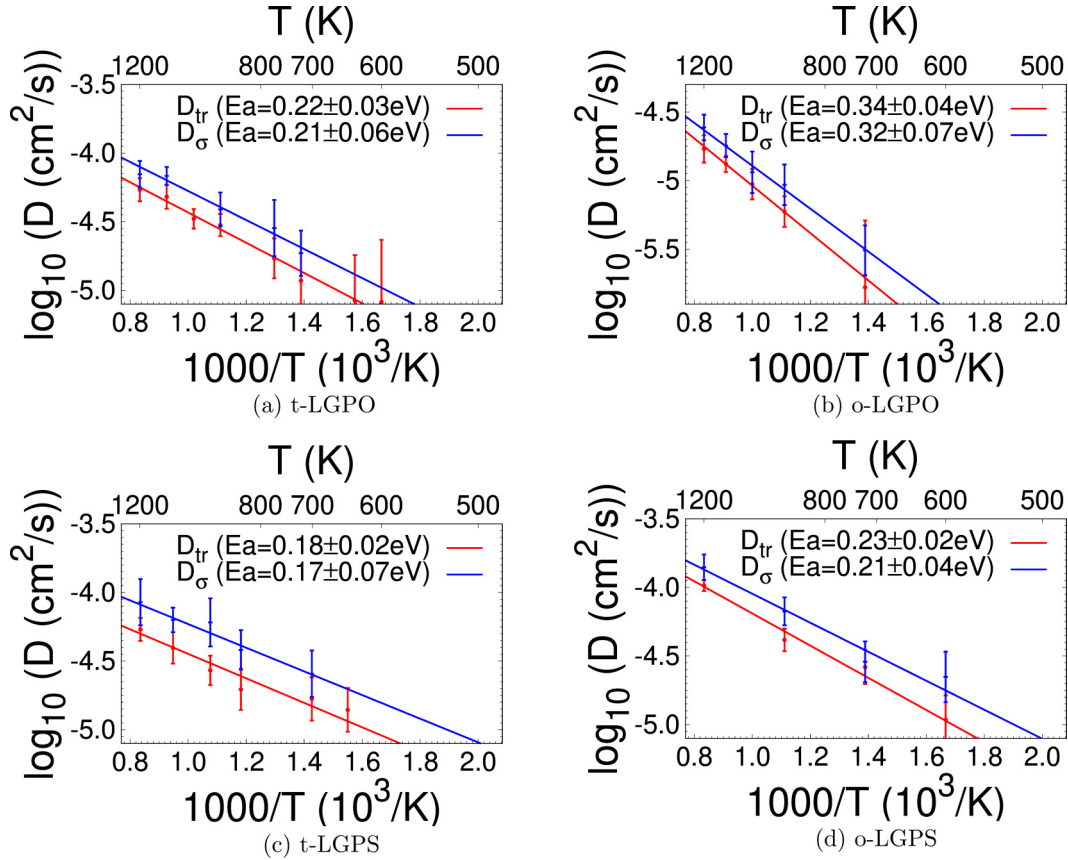|	$E_{a_{D_{\mathrm{tr}}}}$	$E_{a_{D_{\mathrm{tr}}}}$ (Ref. [96])	$E_{a_{D_\sigma}}$	$E_{a_{\sigma T}}$ (expt.)
t-LGPO	0.22 ± 0.03	0.36 ± 0.05	0.21 ± 0.06	
o-LGPO	0.34 ± 0.04		0.32 ± 0.07	0.53 [120]
t-LGPS	0.18 ± 0.02	0.21 ± 0.04	0.17 ± 0.07	0.25 [80]
o-LGPS	0.23 ± 0.02		0.21 ± 0.04	0.24 [66]

FIG. 4.   (a): Arrhenius plots for Li-ion charge diffusion [D_{σ}^{Li}, Eq. (6)] in t-LGPO from NVT CP molecular dynamics, compared with t-LGPO Li-ion tracer diffusion [$D_{\text{tr}}^{\text{Li}}$, Eq. (3), reported in Fig. 3], to estimate the role of the ionic correlation (Haven ratio) [124]. For completeness, in (b), (c), and (d), we report the same quantities for o-LGPO, t-LGPS, and o-LGPS, respectively (see also Ref. [124]).

IV. DYNAMICAL PHASE STABILITY OF t-LGPO

In this section, we aim to get insights into the stability of the hypothetical tetragonal t-LGPO. For this purpose, we study its dynamical stability by means of variable-cell molecular dynamics at controlled temperature (NPT ensemble), which we compare to the same simulations for the existing orthorhombic phase [122], o-LGPO. Furthermore, we exploit dynamical ionic configurations extracted from the NPT molecular dynamics to explore hypothetical conditions favoring a phase transition from o-LGPO to t-LGPO.

A. Phase stability from *NPT* simulations

The electronic total energy and volume per formula unit during the NPT CP simulations [144,145] of t-LGPO at 600 K (for details, see Sec. S VI of the Supplemental Material [125] and references therein) are displayed in Fig. 5, together with the same quantities for the o-LGPO dynamics. As a further comparison, we perform the same simulations for t-LGPS and o-LGPS, and we report energies and volumes in Fig. 6. One formula unit here is $Li_{10}GeP_2O_{12}$ or $Li_{10}GeP_2S_{12}$, i.e., 25 atoms. In Table II we report the mean values from the 600 K-NPT molecular dynamics for geometries, electronic total energies, and enthalpies. For all systems, the average internal pressure during the dynamics is of the order of 10^{-2} GPa or less.

From Fig. 5(a), the electronic total energy of t-LGPO sits clearly above o-LGPO, as also reported in Table II for $\langle E_{\text{tot}} \rangle$ and $\langle H \rangle$. The trend $\langle E_{\text{tot}} \rangle$(o-LGPO) $< \langle E_{\text{tot}} \rangle$(t-LGPO) is observed systematically also in the NVT simulations of Sec. III (results not shown here), but the NPT simulations show in addition that this trend is unchanged, at least at 600 K, even if the cell is allowed to vary its volume and shape (of course, we compare here $\langle E \rangle$, but the thermodynamic functional is the Gibbs free energy $G = E - TS + PV$). On the contrary, for the sulfide system [Fig. 6(a)] the orthorhombic and tetragonal phases show similar energetics. The NPT simulations for t-LGPO and o-LGPO can be taken as a further confirmation that the formation of a tetragonal phase of LGPO would be less favored against the orthorhombic phase [122], as shown by the fact that partial oxygen substitution was possible in tetragonal LGPS only up to $x = 0.9$ in $Li_{10}GeP_2S_{(12-x)}O_x$ [115]. However, from Fig. 5 we also note that, during 200 ps dynamics at 600 K, neither the total energy nor the volume of t-LGPO undergo changes that might indicate ongoing phase transitions.

On the side of the cell geometry, the volume fluctuations for t-LGPO are larger than for o-LGPO [Fig. 5(b) and Table II]. It can be noted that in the case of LGPS instead [Fig. 6(b) and Table II] they have comparable amplitudes for t-LGPS and o-LGPS. Also, the in-plane lattice parameters a and b display stronger oscillations in t-LGPO than in t-LGPS (Table II), the former showing a larger fractional difference
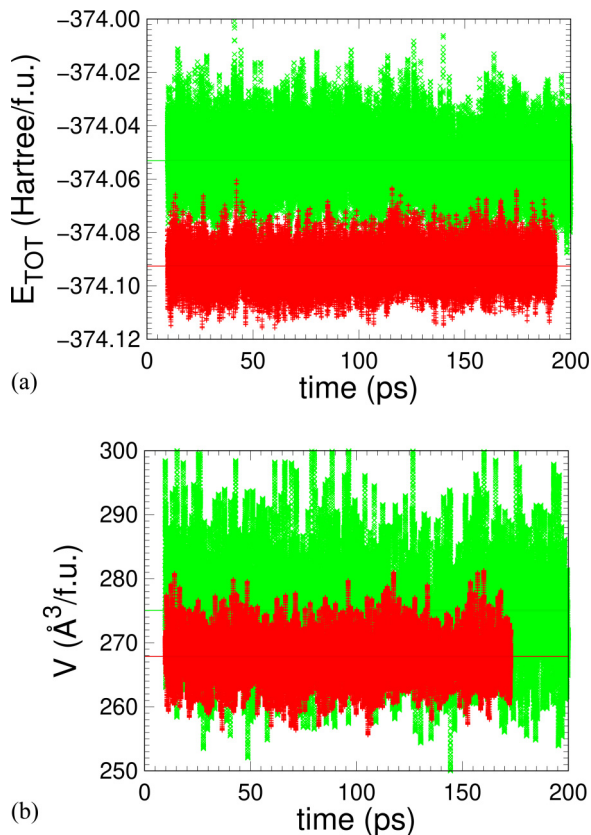
FIG. 5. 600 K-*NPT* CP molecular dynamics for t-LGPO (green points) and o-LGPO (red points): (a) Electronic total energy per formula unit (25 atoms); (b) volume per formula unit. See also Table II.
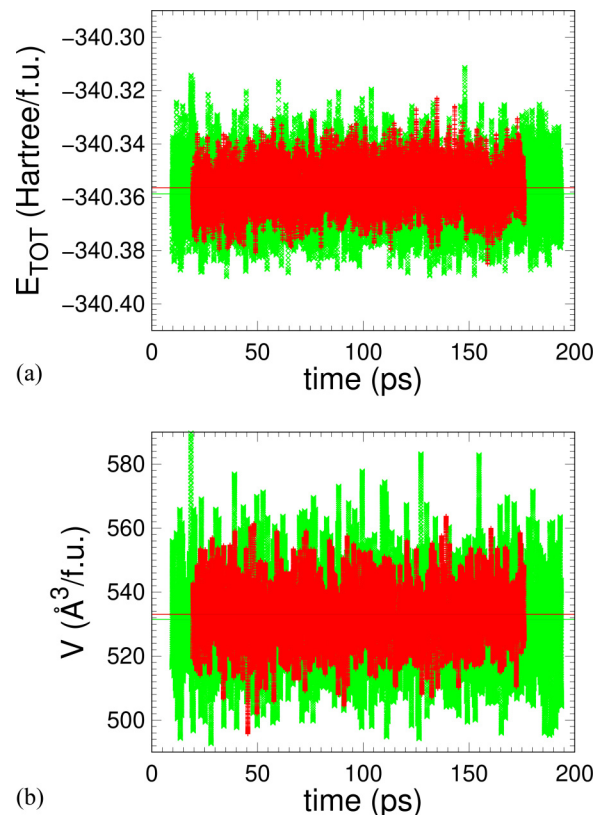

FIG. 6. 600 K-*NPT* CP molecular dynamics for t-LGPS (green points) and o-LGPS (red points): (a) Electronic total energy per formula unit (25 atoms); (b) volume per formula unit. See also Table II.

between $\langle a \rangle$ and $\langle b \rangle$ than the latter (0.7% instead of 0.09%). These results point to a slight deviation from tetragonality for the oxide, with the simulations happy to switch between two slightly nontetragonal equivalent forms. In Fig. 7 we show a, b, and c for the 50-atom t-LGPO supercell described above and for the 200-atom ($2 \times 2 \times 1$) t-LGPO supercell that we also simulate (*NPT*, 100 ps) for this purpose: while a and b often switch in the 50-atom supercell [Fig. 7(a)], in the 200-atom cell simulation these fluctuations are suppressed [Fig. 7(b)], but a and b stabilize at two fairly different values ($\langle ||b - a|| \rangle \sim 1$ Å).

B. Possible conditions for a phase transition from o-LGPO to t-LGPO

The *NVT* results for Li-ion diffusion in t-LGPO (Sec. III and Figs. 3 and 4) show that one could in principle obtain the same Li-ion diffusion in the oxide analog of t-LGPS (t-LGPO) as in o-LGPS or t-LGPS. However, results from the *NPT* simulations presented in this section [Fig. 5(a) and Table II] reiterate that this phase, though dynamically stable over 200 ps, is less favored with respect to its orthorhombic allotrope o-LGPO [119,122]. It thus becomes appealing to investigate the possibility of a transition from the more stable and less conductive o-LGPO to the metastable and more conductive t-LGPO. Neglecting entropy, a first step in such an

TABLE II. Average lattice parameters, angles, volumes, total energies, and enthalpies from 600 K-*NPT* CP molecular dynamics for t-LGPO (first line) and for the benchmark structures o-LGPO, t-LGPS, and o-LGPS (following lines). Lengths are in Å, angles in degrees, and energies in Hartree per formula unit. Formula units contain 25 atoms: $Li_{10}GeP_2O_{12}$ for t- and o-LGPO, and $Li_{10}GeP_2S_{12}$ for t- and o-LGPS (in the calculations, tetragonal supercells contain 50 atoms and orthorhombic supercells contain 100 atoms). Errors are calculated as mean standard deviations in a block analysis, as done for diffusion (see Sec. S IV in the Supplemental Material [125] and Refs. [149,151]). See also Figs. 5 and 6.

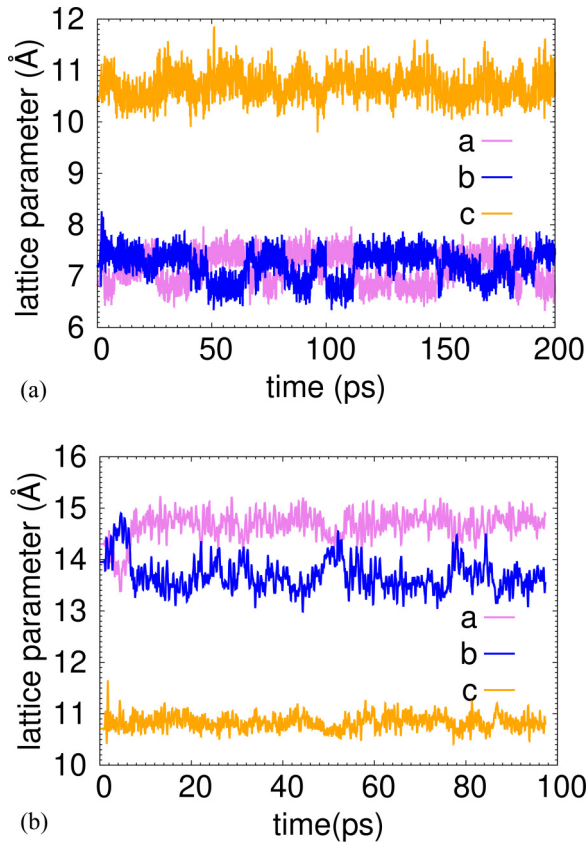|	$\langle a \rangle$	$\langle b \rangle$	$\langle c \rangle$	$\langle \alpha \rangle$	$\langle \beta \rangle$	$\langle \gamma \rangle$	$\langle V \rangle$	$\langle E_{tot} \rangle$	$\langle H \rangle$
t-LGPO	7.15 ± 0.31	7.20 ± 0.30	10.72 ± 0.27	90.1 ± 2.2	90.0 ± 2.1	90.1 ± 1.3	275.0 ± 7.1	-374.053 ± 0.010	-374.055 ± 0.087
o-LGPO	10.69 ± 0.12	6.50 ± 0.08	15.42 ± 0.18	90.0 ± 0.8	89.9 ± 1.0	90.1 ± 0.9	267.9 ± 3.5	-374.092 ± 0.007	-374.093 ± 0.059
t-LGPS	9.01 ± 0.18	9.01 ± 0.18	13.12 ± 0.25	90.0 ± 2.3	89.9 ± 2.3	90.1 ± 1.7	531.5 ± 13.4	-340.359 ± 0.010	-340.361 ± 0.072
o-LGPS	12.85 ± 0.20	8.86 ± 0.12	18.72 ± 0.27	90.1 ± 1.1	90.1 ± 1.8	90.1 ± 1.3	533.0 ± 8.8	-340.356 ± 0.007	-340.357 ± 0.053

FIG. 7. Lattice parameters for t-LGPO during the 600 K-*NPT* CP molecular dynamics: (a) 50-atom supercell simulation (see also Table II); (b) 200-atom ($2 \times 2 \times 1$) supercell simulation (see the text).

investigation is to extract representative configurations from the *NPT* dynamics of the two LGPO phases and construct equations of state $E_{tot}(V)$ by isotropically compressing and expanding the cells at each of these configurations. The location of a possible crossing between a t-LGPO and an o-LGPO $E_{tot}(V)$ would suggest whether compression or expansion could induce a transition from o-LGPO to t-LGPO or *vice versa*. A set of 16 such equations of state (8 for t-LGPO and 8 for o-LGPO) is displayed in Fig. 8(a). For each phase, the eight configurations are chosen uniformly in the range of E_{tot} [Fig. 5(a)] and for each configuration the maximum expansion/compression of the cell volume is ±10%. In addition, we fit the values of $E_{tot}(V)$ in Fig. 8(a) to a Murnaghan equation of state [132,160,161], from which we calculate the pressure p and the enthalpy H. The enthalpy-pressure curves are reported in Fig. 8(b). From both the energy-volume and enthalpy-pressure curves (Fig. 8), it is not straightforward to get unambiguous information about whether a cell compression or expansion could help a transition between t-LGPO and o-LGPO: in particular, in Fig. 8(b) one can see that in general the enthalpies have a similar slope, as a function of pressure, in the two phases. We can extract the same information directly from the *NPT* dynamics (Sec. IV A). In Fig. 9 we report the enthalpy-pressure data sampled at every 20 time steps of the *NPT* simulations of Fig. 5 for o-LGPO and t-LGPO, together with a linear fit for each phase. It is clear that t-LGPO
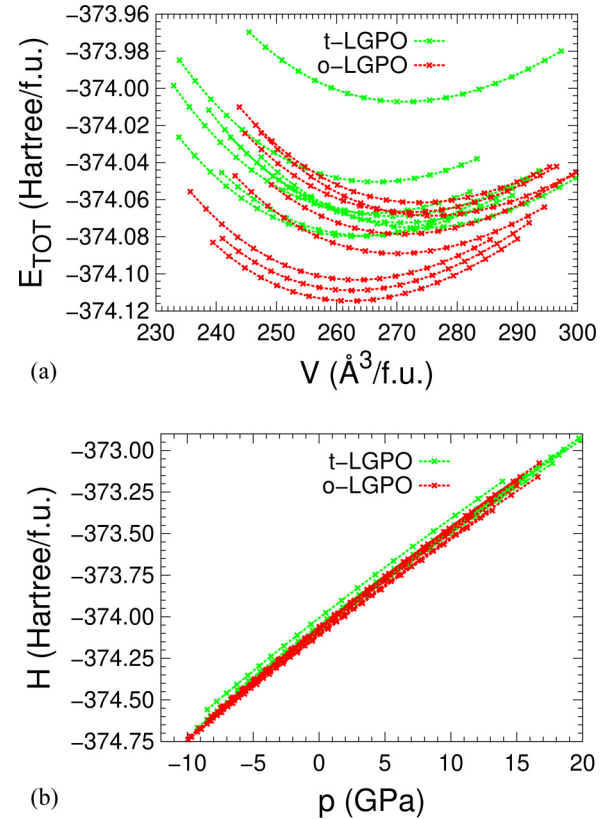

FIG. 8. (a) Energy-volume $E_{tot}(V)$ equations of state (crosses), and corresponding Murnaghan [161] fits (dashed lines), obtained by isotropically expanding and compressing eight configurations of t-LGPO and o-LGPO (in green and red, respectively), extracted from the 600 K-*NPT* CP dynamics (Fig. 5). (b) Enthalpy-pressure $H(p)$ relations for the same configurations of t-LGPO (green curves) and o-LGPO (red curves), from the Murnaghan fits in (a).

has univocally a higher enthalpy than o-LGPO for an extended range of pressures. Figure 9 might show that this trend could be inverted at $p \ll 0$, so that an expansion should favor the tetragonal phase more than a compression, but in general
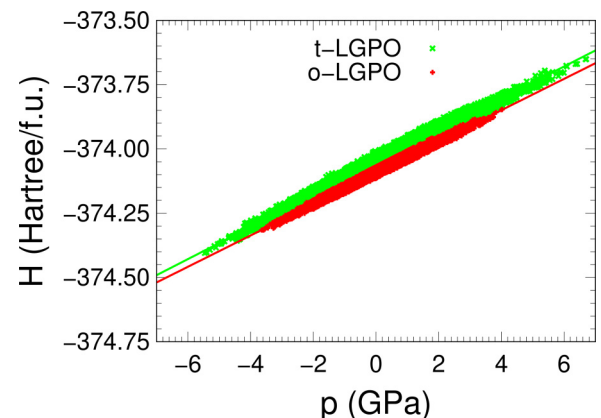

FIG. 9. Enthalpy-pressure relation obtained directly from the values of enthalpy and pressure during the 600 K-*NPT* CP simulations of t-LGPO and o-LGPO (Fig. 5). t-LGPO and o-LGPO results are reported in green and red, respectively.
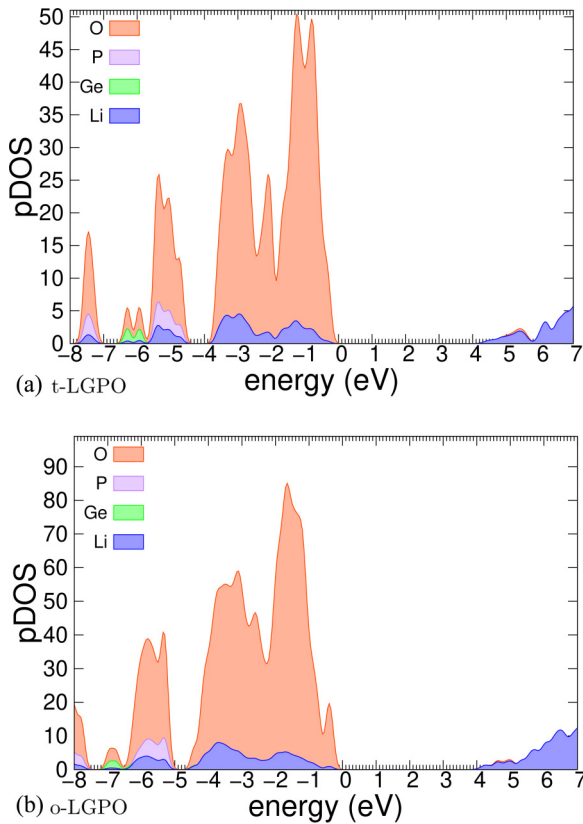
FIG. 10. Projected electronic density of states (pDOS) for (a) t-LGPO and (b) o-LGPO at the PBE level from the converged SCF density at relaxed geometry with full **k**-points sampling (see Table I in the Supplemental Material [125]). In the calculations, the number of bands is ∼20% larger than the number of filled bands. Energies are reported with respect to the highest occupied level. A Kohn-Sham band gap larger than 4 eV is present.
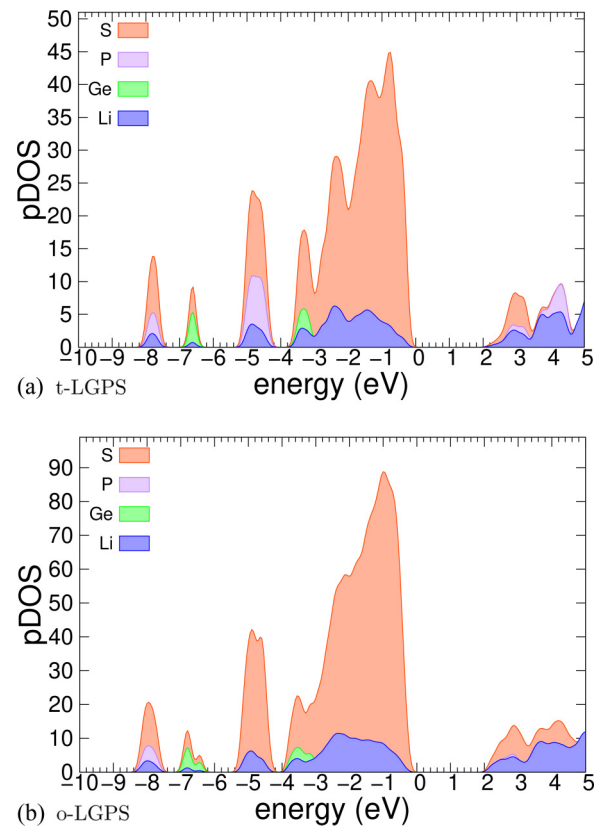

FIG. 11. Same as Fig. 10 for (a) t-LGPS and (b) o-LGPS, to provide a comparison to the sulfide analog of t- (o-) LGPO. Energies are reported with respect to the highest occupied level. A Kohn-Sham band gap of ∼2 eV is present, implying that t- (o-) LGPO (Fig. 10) is expected to show a superior electrochemical stability window with respect to LGPS.

the enthalpy cost, if ascribed entirely to the 10 Li atoms in the formula unit, is around 100 meV/at (see Table II), i.e., affordable at temperatures of ∼1100 K. Eventually, considering the free energy $G = H - TS$, one should stress that the entropic contribution, stronger for the more diffusive phase, could tilt the thermodynamic balance in favor of t-LGPO at large enough temperatures.

V. t-LGPO BAND GAP AND ELECTROCHEMICAL STABILITY

The band gap of a superionic material is a useful property that gives an estimate of its electrochemical window of stability as a solid-state electrolyte [11]. We calculate band structures and electronic densities of states (DOS) at the Kohn-Sham PBE level (thus, they are only qualitatively accurate), and we evaluate band gaps for LGPO in both the hypothetical tetragonal (t-LGPO) and the existing LISICON (o-LGPO) phases. As our aim is mainly qualitative, it is interesting to report the same investigation also for t-LGPS and o-LGPS in order to provide a comparative evaluation of the electrochemical performance of these oxide and sulfide systems as electrolytes in a battery. In Figs. 10 and 11, the projected DOS (p-DOS, i.e., the DOS projected over the

different n, l, and m components and then summed for any given species) are displayed for LGPO and LGPS, respectively, both in the tetragonal and orthorhombic phases. The p-DOS displayed are taken from the converged SCF density at the relaxed geometry with fully converged **k**-point sampling (see Table I in the Supplemental Material [125]), but very similar results were obtained from the Γ-point relaxed geometry (band gaps converged within 0.1 eV). A number of bands ∼20% larger than the number of filled bands is used (302 and 151 bands for the orthorhombic and tetragonal phases, respectively). Our calculations show that t- and o-LGPO, having about twice the band gap with respect to the sulfides t- and o-LGPS, are thus expected to have significantly larger electrochemical stability windows. Our findings are supported by the aforementioned experimental results reporting a 9 V electrochemical stability window for the orthorhombic oxychloride $Li_{10}Si_{1.5}P_{1.5}Cl_{0.5}O_{11.5}$ [121] and a 5 V electrochemical stability window for the tetragonal oxysulfide $Li_{(3+5x)}P_{(1-x)}S_{(4-z)}O_z$ [110], and also by previous calculations comparing t-LGPO and t-LGPS [96].

VI. DISCUSSION

Table I reports the activation energy E_a [Eq. (9)] for Li-ion diffusion in t-LGPO, against the same quantity calculated for
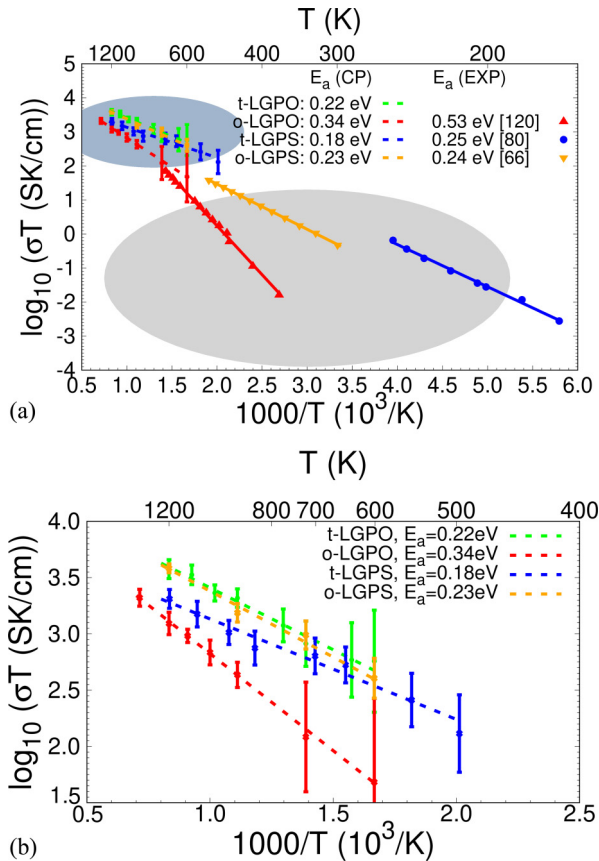
FIG. 12. (a) Arrhenius plots for σT [Li-ion conductivity σ from Eq. (5) multiplied by T] and activation energies from Eq. (9) in t-LGPO, o-LGPO, t-LGPS, and o-LGPS from the CP simulations (Sec. III), compared with the experimental results for o-LGPO and the sulfides. In Eq. (5) we use the tracer diffusion coefficients D_{tr} [Eq. (3) and Fig. 3]. CP simulations (here) and experiments (Refs. [66,80,120]) are highlighted in the blue-gray and light-gray ovals, respectively. (b) Enlargement of (a) for the CP simulations.

o-LGPO, t-LGPS, and o-LGPS. For the latter three benchmark phases, in Table I we compare E_a to experimental results [66,80,120]. To compare not only E_a but also the full conductivity profile, we calculate σ from Eq. (5) [with $D_{\text{tr}}^{\text{Li}}$ from Eq. (3); see also Fig. 3], and we report in Fig. 12(a) the σT Arrhenius plots for t-LGPO and for the three benchmark systems o-LGPO, t-LGPS, and o-LGPS, which we contrast with their experimental σT Arrhenius plots from Refs. [66,80,120]. For o-LGPO and t-LGPS, we note a similar underestimation (~60–70 %) of the activation barrier with respect to the experiments [78,80,120,123], which might be related to the different ranges of temperatures covered—our results being at 500–1200 K and the experimental results at 150–700 K. For o-LGPS the activation barrier for conductivity is in close agreement with the experimental value, whereas the absolute values of $\log_{10}(\sigma T)$ are systematically higher [see Fig. 12(a)]. The latter result is likely related to the differences between the cell of Ref. [66] and the LGPS-adapted o-LGPO cell (see Sec. II A), which we simulate here because structural

details of the genuine thio-LISICON II ($0.6 < x < 0.8$) phase of $\text{Li}_{(4-x)}\text{Ge}_{(1-x)}\text{P}_x\text{S}_4$ [66] are not available (see also [79]). Finally, it should be noted that many physical parameters can affect the bulk ionic conductivity in impedance spectroscopy measurements [162], that the polycrystalline texture of the samples introduces many grain-boundary effects, and that on the computational side the Nernst-Einstein equation [Eq. (5)], even including Haven ratios [163] and the effects of the ionic correlations [Eq. (8), [124]], assumes the oxidation number of the Li atoms to be constant ($Z = +1$) during the dynamics [152,153]. Comparison with the experimental results should thus be regarded as a guide rather than an ultimate benchmark. Nevertheless, extrapolating the o-LGPO, t-LGPS, and o-LGPS results at room temperature, we still reproduce the experimentally observed rank $\sigma(\text{o-LGPO}) \ll \sigma(\text{o-LGPS}) < \sigma(\text{t-LGPS})$ [66,78,80,120,123]. We conclude that the present results, in good agreement with the available experimental literature for what concerns the absolute conductivities of each of the experimentally known phases, also reproduce well their conductivity trend [Fig. 12(a) and Table I].

The agreement of theoretical and experimental conductivities for the benchmark, experimentally known LGPO and LGPS phases, can serve as the foundation to discuss ionic conductivity in t-LGPO, which is the main target of investigation of the present work. In Fig. 12(b) an enlargement of the computational results displayed in Fig. 12(a) is reported. t-LGPO would be a very conductive material, with a σT Arrhenius behavior very similar to that of o-LGPS. Interestingly enough, we find an activation barrier of 0.22 eV, which is very close to the theoretical activation barriers of 0.18 and 0.23 eV for t-LGPS and o-LGPS, respectively, and much smaller than the activation energy of 0.34 eV for o-LGPO [see Table I and Fig. 12(b)]. This finding is at variance with the diffusion results for t-LGPO from a previous first-principles calculation [96], where Li-ion diffusivity in this system is reported to be significantly lower and with a higher activation barrier than in t-LGPS (see Ref. [96] and Table I), but in agreement with the diffusion results for t-LGPO from an *ab initio* trained frozen-lattice potential (pinball) method [159].

t-LGPO, though remaining stable in a 200 ps simulation, is thermodynamically unfavorable with respect to o-LGPO [Figs. 5(a) and 9], and in fact only o-LGPO has been synthesized so far [119,120,122,123]. A solid solution starting from t-LGPS ($\text{Li}_{10}\text{GeP}_2\text{S}_{(12-x)}\text{O}_x$) was shown to be stable only up to $x = 0.9$ [115], showing that preparing t-LGPO via solid-solution synthesis does not seem to be a feasible method, due to the difference in ionic radii between oxygen and sulfur [see also Figs. 5(b) and 6(b)]. In the case of the solid solution $\text{Li}_{(3+5x)}\text{P}_{(1-x)}\text{S}_{(4-z)}\text{O}_z$, a highly conductive tetragonal structure has been obtained up to $z = 0.8$ thanks to rapid quenching of the molten mixture from $T > 700$ °C [110]. A totally different procedure would be to start from the experimental o-LGPO [119,120,122,123] and try to induce a phase transition from orthorhombic to tetragonal by either imposing a negative hydrostatic pressure or introducing a tensile in-plane strain via epitaxial growth, as pointed out in Sec. IV B (see also [164]). Most importantly, entropy, being in principle higher for the more conductive phase t-LGPO, could tilt the thermodynamic balance between the two phases. We leave the latter consideration to a further study.

VII. SUMMARY AND CONCLUSIONS

Sulfide crystalline lithium ionic conductors, in particular tetragonal LGPS [78,81] and the thio-LISICON family [66,71–77], have shown optimal conductive properties that are in general superior to the originally proposed oxides in the LISICON family [47–54]. However, they also display severe practical hindrances [165], such as the need to strictly control the atmosphere in which they are processed in order to avoid releasing toxic H_2S [107] and consequent degradation in conductivity [166], and a generally weak chemical and electrochemical stability [98,103,104,106]. Recent experimental work shows that H_2S generation is significantly suppressed after adding Li_2O or P_2O_5 to the Li_2O-Li_2S-P_2S_5 glass [73,114], and that oxygen-substituted LGPS-like materials display a much better chemical and electrochemical stability than pure sulfides [115–117]. In this respect, new investigations on the oxide-analog crystalline materials, potentially less conductive but displaying superior safety and stability features, are highly desirable, and a new wave of investigations has been recently directed toward the genuine LISICON orthorhombic Li-Ge-P-O system [120,167–169].

In this paper, we study the ionic conductivity and dynamical stability of $Li_{10}GeP_2O_{12}$ (LGPO) in a hypothetical tetragonal phase (t-LGPO), i.e., the oxide analog of tetragonal LGPS [78,80], with the aim of investigating a potentially fast and safe ionic conductor. As a comparison, we provide a parallel study for the corresponding LGPO orthorhombic phase, and for thio-LISICON and tetragonal LGPS. LGPS has been extensively studied so far, both experimentally [78,80,81,84,90,91,93,101,104,170,171] and theoretically [79,94–96,99,100,124,172,173], in its highly conductive tetragonal phase (space group $P4_2/nmc$, $\sigma = 1.2 \times 10^{-2}$ S cm^{-1} at room temperature [78], here denoted t-LGPS), but it is known from experiments to exist also in its monoclinic allotrope (thio-LISICON [66], here approximated by the o-LGPS structure), which also shows high conductivity ($\sigma \sim 10^{-3}$ S cm^{-1} at room temperature) and whose structure is related to the orthorhombic parent lattices Li_4GeS_4 and Li_3PS_4 [66]. On the other hand, LGPO is known from experiments to exist in its moderately conducting (1.8×10^{-6} S cm^{-1} at 40 °C [120,123]) LISICON orthorhombic phase (space group *Pnma*, here denoted o-LGPO) [51,119,120,122,123], which has also been studied in simulations using classical molecular dynamics [168] and machine-learning techniques [174], but no experimental evidence of a LGPS-analog tetragonal phase (t-LGPO), which is the main focus of this work, has been reported in the literature so far.

We have performed extensive Car-Parrinello molecular dynamics simulations (plane waves, ultrasoft pseudopotentials [132]) in the NVT ensemble at temperatures between 600 and 1200 K to calculate Li-ion diffusion and conductivity of t-LGPO. Further, we provide Car-Parrinello variable-cell [145] NPT simulations at $T = 600$ K to investigate the dynamical stability of t-LGPO. We have performed the same simulations also for the experimentally known o-LGPO and t-LGPS phases, and for the o-LGPS structure, which we included as a close approximation to the quasi-orthorhombic thio-LISICON II phase of Ref. [66]. Results for the conductivity of these experimentally known phases agree well with the experiments. t-LGPO, the oxide-analog of t-LGPS (which has not been synthesized so far), reveals itself to be a fast ionic conductor, with an Arrhenius behavior of the Li-ion conductivity similar to that in o-LGPS and a conductivity at room temperature comparable to the conductivities of o- and t-LGPS. In addition, t-LGPO, being an oxide, is not expected to carry the stability problems encountered in sulfide electrolytes [165] for solid-state batteries, and it could represent a relevant and important challenge for experimental synthesis and stabilization.

[1] V. Arunachalam and E. Fleischer, MRS Bull. **33**, 264 (2008).

[2] G. L. Kyriakopoulos and G. Arabatzis, Renew. Sustain. Energy Rev. **56**, 1044 (2016).

[3] Z. Yang, J. Liu, S. Baskaran, C. H. Imhoff, and J. D. Holladay, JOM **62**, 14 (2010).

[4] Z. Yang, J. Zhang, M. C. Kintner-Meyer, X. Lu, D. Choi, J. P. Lemmon, and J. Liu, Chem. Rev. **111**, 3577 (2011).

[5] S. F. Tie and C. W. Tan, Renew. Sustain. Energy Rev. **20**, 82 (2013).

[6] Meet powerwall, your home battery, https://www.tesla.com/powerwall, accessed: 2020-07-04.

[7] M. Yoshino, S. Yoneyama, O. Kimura, T. Ohsawa, and T. Kabata, Secondary battery (1991), U.S. Patent 5,037,713.

[8] T. Nagaura and K. Tozawa, Prog. Batteries Sol. Cells **9**, 209 (1990).

[9] G. E. Blomgren, J. Electrochem. Soc. **164**, A5019 (2017).

[10] P. Poizot and F. Dolhem, Energy Environ. Sci. **4**, 2003 (2011).

[11] J. B. Goodenough and K.-S. Park, J. Am. Chem. Soc. **135**, 1167 (2013).

[12] M. Winter and R. J. Brodd, Chem. Rev. **104**, 4245 (2004).

[13] D. Larcher and J.-M. Tarascon, Nat. Chem. **7**, 19 (2015).

[14] A. Kwade, W. Haselrieder, R. Leithoff, A. Modlinger, F. Dietrich, and K. Droeder, Nat. Energy **3**, 290 (2018).

[15] E. A. Olivetti and J. M. Cullen, Science **360**, 1396 (2018).

[16] M. S. Whittingham, Science **192**, 1126 (1976).

[17] J. B. Goodenough and Y. Kim, Chem. Mater. **22**, 587 (2009).

[18] S. Goriparti, E. Miele, F. De Angelis, E. Di Fabrizio, R. P. Zaccaria, and C. Capiglia, J. Power Sources **257**, 421 (2014).

[19] P. Rozier and J. M. Tarascon, J. Electrochem. Soc. **162**, A2490 (2015).

[20] R. Fong, U. Von Sacken, and J. R. Dahn, J. Electrochem. Soc. **137**, 2009 (1990).

[21] K. Xu, Chem. Rev. **104**, 4303 (2004).

[22] B. C. Melot and J.-M. Tarascon, Acc. Chem. Res. **46**, 1226 (2013).

[23] M. S. Whittingham, Chem. Rev. **104**, 4271 (2004).

[24] K. Mizushima, P. Jones, P. Wiseman, and J. B. Goodenough, Mater. Res. Bull. **15**, 783 (1980).

[25] D. Liu, W. Zhu, J. Trottier, C. Gagnon, F. Barray, A. Guerfi, A. Mauger, H. Groult, C. Julien, J. Goodenough, and K. K. Zaghib, RSC Adv. **4**, 154 (2014).

[26] A. K. Padhi, K. S. Nanjundaswamy, and J. B. Goodenough, J. Electrochem. Soc. **144**, 1188 (1997).

[27] M. M. Thackeray, S.-H. Kang, C. S. Johnson, J. T. Vaughey, R. Benedek, and S. Hackney, J. Mater. Chem. **17**, 3112 (2007).

[28] Y. Wang, J. Jiang, and J. Dahn, Electrochem. Commun. **9**, 2534 (2007).

[29] H. Shigemura, M. Tabuchi, H. Kobayashi, H. Sakaebe, A. Hirano, and H. Kageyama, J. Mater. Chem. **12**, 1882 (2002).

[30] D. MacNeil and J. R. Dahn, J. Electrochem. Soc. **149**, A912 (2002).

[31] G. Amatucci, C. Schmutz, A. Blyr, C. Sigala, A. Gozdz, D. Larcher, and J. Tarascon, J. Power Sources **69**, 11 (1997).

[32] R. Dedryvere, D. Foix, S. Franger, S. Patoux, L. Daniel, and D. Gonbeau, J. Phys. Chem. C **114**, 10999 (2010).

[33] A. Hammami, N. Raymond, and M. Armand, Nature (London) **424**, 635 (2003).

[34] P. Knauth and H. L. Tuller, J. Am. Ceram. Soc. **85**, 1654 (2002).

[35] P. Knauth, Solid State Ion. **180**, 911 (2009).

[36] E. Quartarone and P. Mustarelli, Chem. Soc. Rev. **40**, 2525 (2011).

[37] J. G. Kim, B. Son, S. Mukherjee, N. Schuppert, A. Bates, O. Kwon, M. J. Choi, H. Y. Chung, and S. Park, J. Power Sources **282**, 299 (2015).

[38] J. Li, C. Ma, M. Chi, C. Liang, and N. J. Dudney, Adv. Energy Mater. **5**, 1401408 (2015).

[39] Y.-S. Hu, Nat. Energy **1**, 16042 (2016).

[40] A. Manthiram, X. Yu, and S. Wang, Nat. Rev. Mater. **2**, 16103 (2017).

[41] M. Braga, N. Grundish, A. Murchison, and J. Goodenough, Energy Environ. Sci. **10**, 331 (2017).

[42] C. Jiang, H. Li, and C. Wang, Sci. Bull. **62**, 1473 (2017).

[43] Z. Gao, H. Sun, L. Fu, F. Ye, Y. Zhang, W. Luo, and Y. Huang, Adv. Mater. **30**, 1705702 (2018).

[44] J. Bates, N. Dudney, G. Gruzalski, R. Zuhr, A. Choudhury, C. Luck, and J. Robertson, J. Power Sources **43**, 103 (1993).

[45] A. Hayashi, A. Sakuda, and M. Tatsumisago, Front. Energy Res. **4**, 25 (2016).

[46] A. Sakuda, A. Hayashi, and M. Tatsumisago, Sci. Rep. **3**, 2261 (2013).

[47] R. Shannon, B. Taylor, A. English, and T. Berzins, in *International Symposium on Solid Ionic and Ionic-Electronic Conductors* (Elsevier, Amsterdam, 1977), pp. 783–796.

[48] H.-P. Hong, Mater. Res. Bull. **13**, 117 (1978).

[49] P. G. Bruce and A. R. West, Mater. Res. Bull. **15**, 379 (1980).

[50] P. G. Bruce and A. R. West, J. Solid State Chem. **44**, 354 (1982).

[51] A. R. Rodger, J. Kuwano, and A. R. West, Solid State Ion. **15**, 185 (1985).

[52] I. Abrahams, P. G. Bruce, A. R. West, and W. David, J. Solid State Chem. **75**, 390 (1988).

[53] I. Abrahams, P. G. Bruce, W. David, and A. R. West, Acta Crystallogr. Sect. B **45**, 457 (1989).

[54] P. G. Bruce, I. Abrahams, and A. R. West, Solid State Ion. **40**, 293 (1990).

[55] J. Zemann, Acta Crystallogr. **13**, 863 (1960).

[56] A. R. West, Z. Kristallogr.-Cryst. Mater. **141**, 422 (1975).

[57] A. R. West and P. G. Bruce, Acta Crystallogr. Sect. B **38**, 1891 (1982).

[58] M. O'Keeffe and B. Hyde, Acta Crystallogr. Sect. B **34**, 3519 (1978).

[59] H. Völlenkle, A. Wittmann, and H. Nowotny, Monatsh. Chem./Chem. Monthly **99**, 1360 (1968).

[60] G. Dittmar and H. Schäfer, Acta Crystallogr. Sect. B **32**, 2726 (1976).

[61] D. Tranqui, R. Shannon, H.-Y. Chen, S. Iijima, and W. Baur, Acta Crystallogr. Sect. B **35**, 2479 (1979).

[62] W. H. Baur, Mater. Res. Bull. **16**, 339 (1981).

[63] I. Abrahams and P. G. Bruce, Acta Crystallogr. Sect. B **47**, 696 (1991).

[64] A. R. West, J. Appl. Electrochem. **3**, 327 (1973).

[65] M. Murayama, R. Kanno, M. Irie, S. Ito, T. Hata, N. Sonoyama, and Y. Kawamoto, J. Solid State Chem. **168**, 140 (2002).

[66] R. Kanno and M. Murayama, J. Electrochem. Soc. **148**, A742 (2001).

[67] R. Mercier, J.-P. Malugani, B. Fahys, G. Robert, and J. Douglade, Acta Crystallogr. Sect. B **38**, 1887 (1982).

[68] M. Tachez, J.-P. Malugani, R. Mercier, and G. Robert, Solid State Ion. **14**, 181 (1984).

[69] K. Homma, M. Yonemura, T. Kobayashi, M. Nagao, M. Hirayama, and R. Kanno, Solid State Ion. **182**, 53 (2011).

[70] R. Kanno, T. Hata, Y. Kawamoto, and M. Irie, Solid State Ion. **130**, 97 (2000).

[71] F. Mizuno, A. Hayashi, K. Tadanaga, and M. Tatsumisago, Solid State Ion. **177**, 2721 (2006).

[72] T. Minami, A. Hayashi, and M. Tatsumisago, Solid State Ion. **177**, 2715 (2006).

[73] T. Ohtomo, A. Hayashi, M. Tatsumisago, and K. Kawamoto, Electrochemistry **81**, 428 (2013).

[74] T. Ohtomo, A. Hayashi, M. Tatsumisago, and K. Kawamoto, J. Solid State Electrochem. **17**, 2551 (2013).

[75] M. Tatsumisago, M. Nagao, and A. Hayashi, J. Asian Ceram. Soc. **1**, 17 (2013).

[76] M. Murayama, R. Kanno, Y. Kawamoto, and T. Kamiyama, Solid State Ion. **154**, 789 (2002).

[77] M. Murayama, N. Sonoyama, A. Yamada, and R. Kanno, Solid State Ion. **170**, 173 (2004).

[78] N. Kamaya, K. Homma, Y. Yamakawa, M. Hirayama, R. Kanno, M. Yonemura, T. Kamiyama, Y. Kato, S. Hama, K. Kawamoto *et al.*, Nat. Mater. **10**, 682 (2011).

[79] S. Adams and R. P. Rao, J. Mater. Chem. **22**, 7687 (2012).

[80] A. Kuhn, V. Duppel, and B. V. Lotsch, Energy Environ. Sci. **6**, 3548 (2013).

[81] A. Kuhn, J. Köhler, and B. V. Lotsch, Phys. Chem. Chem. Phys. **15**, 11620 (2013).

[82] P. Bron, S. Johansson, K. Zick, J. Schmedt auf der Günne, S. Dehnen, and B. Roling, J. Am. Chem. Soc. **135**, 15694 (2013).

[83] A. Kuhn, O. Gerbig, C. Zhu, F. Falkenberg, J. Maier, and B. V. Lotsch, Phys. Chem. Chem. Phys. **16**, 14669 (2014).

[84] Y. Kato, R. Saito, M. Sakano, A. Mitsui, M. Hirayama, and R. Kanno, J. Power Sources **271**, 60 (2014).

[85] Y. Seino, T. Ota, K. Takada, A. Hayashi, and M. Tatsumisago, Energy Environ. Sci. **7**, 627 (2014).

[86] J. M. Whiteley, J. H. Woo, E. Hu, K.-W. Nam, and S.-H. Lee, J. Electrochem. Soc. **161**, A1812 (2014).

[87] S. Hori, M. Kato, K. Suzuki, M. Hirayama, Y. Kato, and R. Kanno, J. Am. Ceram. Soc. **98**, 3352 (2015).

[88] S. Hori, S. Taminato, K. Suzuki, M. Hirayama, Y. Kato, and R. Kanno, Acta Crystallogr. Sect. B **71**, 727 (2015).

[89] S. Hori, K. Suzuki, M. Hirayama, Y. Kato, T. Saito, M. Yonemura, and R. Kanno, Faraday Discuss. **176**, 83 (2015).

[90] O. Kwon, M. Hirayama, K. Suzuki, Y. Kato, T. Saito, M. Yonemura, T. Kamiyama, and R. Kanno, J. Mater. Chem. A **3**, 438 (2015).

[91] K. Yang, J. Dong, L. Zhang, Y. Li, and L. Wang, J. Am. Ceram. Soc. **98**, 3831 (2015).

[92] Y. Kato, S. Hori, T. Saito, K. Suzuki, M. Hirayama, A. Mitsui, M. Yonemura, H. Iba, and R. Kanno, Nat. Energy **1**, 16030 (2016).

[93] D. A. Weber, A. Senyshyn, K. S. Weldert, S. Wenzel, W. Zhang, R. Kaiser, S. Berendts, J. Janek, and W. G. Zeier, Chem. Mater. **28**, 5905 (2016).

[94] Y. Mo, S. P. Ong, and G. Ceder, Chem. Mater. **24**, 15 (2012).

[95] M. Xu, J. Ding, and E. Ma, Appl. Phys. Lett. **101**, 031901 (2012).

[96] S. P. Ong, Y. Mo, W. D. Richards, L. Miara, H. S. Lee, and G. Ceder, Energy Environ. Sci. **6**, 148 (2013).

[97] N. D. Lepley, N. A. W. Holzwarth, and Y. A. Du, Phys. Rev. B **88**, 104103 (2013).

[98] Y. Zhu, X. He, and Y. Mo, ACS Appl. Mater. Interfaces **7**, 23685 (2015).

[99] Y. Wang, W. D. Richards, S. P. Ong, L. J. Miara, J. C. Kim, Y. Mo, and G. Ceder, Nat. Mater. **14**, 1026 (2015).

[100] Y. Zhu, X. He, and Y. Mo, J. Mater. Chem. A **4**, 3253 (2016).

[101] F. Han, Y. Zhu, X. He, Y. Mo, and C. Wang, Adv. Energy Mater. **6**, 1501590 (2016).

[102] Y. Kato, S. Hori, and R. Kanno, Adv. Energy Mater. **10**, 2002153 (2020).

[103] M. Sakuma, K. Suzuki, M. Hirayama, and R. Kanno, Solid State Ion. **285**, 101 (2016).

[104] S. Wenzel, S. Randau, T. Leichtweiß, D. A. Weber, J. Sann, W. G. Zeier, and J. Janek, Chem. Mater. **28**, 2400 (2016).

[105] F. Han, T. Gao, Y. Zhu, K. J. Gaskell, and C. Wang, Adv. Mater. **27**, 3473 (2015).

[106] B. V. Lotsch and J. Maier, J. Electroceram. **38**, 128 (2017).

[107] Y. S. Jung, D. Y. Oh, Y. J. Nam, and K. H. Park, Isr. J. Chem. **55**, 472 (2015).

[108] Z. Ma, H.-G. Xue, and S.-P. Guo, J. Mater. Sci. **53**, 3927 (2018).

[109] J. Kim, G. Park, K. Lee, H. Park, S. Nam, and S. Song, J. Power Sources **189**, 211 (2009).

[110] K. Suzuki, M. Sakuma, S. Hori, T. Nakazawa, M. Nagao, M. Yonemura, M. Hirayama, and R. Kanno, Solid State Ion. **288**, 229 (2016).

[111] X. Wang, R. Xiao, H. Li, and L. Chen, Phys. Chem. Chem. Phys. **18**, 21269 (2016).

[112] K. Takada, M. Osada, N. Ohta, T. Inada, A. Kajiyama, H. Sasaki, S. Kondo, M. Watanabe, and T. Sasaki, Solid State Ion. **176**, 2355 (2005).

[113] A. Neveu, V. Pelé, C. Jordy, and V. Pralong, J. Power Sources **467**, 228250 (2020).

[114] K. Minami, A. Hayashi, and M. Tatsumisago, Solid State Ion. **179**, 1282 (2008).

[115] Y. Sun, K. Suzuki, K. Hara, S. Hori, T.-a. Yano, M. Hara, M. Hirayama, and R. Kanno, J. Power Sources **324**, 798 (2016).

[116] S. Hori, K. Suzuki, M. Hirayama, Y. Kato, and R. Kanno, Front. Energy Res. **4**, 38 (2016).

[117] K.-H. Kim and S. W. Martin, Chem. Mater. **31**, 3984 (2019).

[118] X. Wang, R. Xiao, H. Li, and L. Chen, Phys. Rev. Lett. **118**, 195901 (2017).

[119] S. Song, Z. Dong, F. Deng, and N. Hu, Funct. Mater. Lett. **11**, 1850039 (2018).

[120] E. Gilardi, G. Materzanini, L. Kahle, M. Döbeli, S. Lacey, X. Cheng, N. Marzari, D. Pergolesi, A. Hintennach, and T. Lippert, ACS Appl. Energy Mater. **3**, 9910 (2020).

[121] S. Song, J. Lu, F. Zheng, H. M. Duong, and L. Lu, RSC Adv. **5**, 6588 (2015).

[122] M. K. Rabadanov, A. Pietraszko, V. Kireev, A. Ivanov-Schitz, and V. Simonov, Crystallogr. Rep. **48**, 744 (2003).

[123] A. Ivanov-Shitz and V. Kireev, Crystallogr. Rep. **48**, 112 (2003).

[124] A. Marcolongo and N. Marzari, Phys. Rev. Mater. **1**, 025402 (2017).

[125] See Supplemental Material at http://link.aps.org/supplemental/10.1103/PhysRevMaterials.5.035408 for additional details (which includes Refs. [175–179]). In particular, see Sec. S I for the relaxed structures details, Sec. S II for the choice of CP parameters, Sec. S III for the thermostat parameters, Sec. S IV for the statistical method to calculate the diffusion coefficients, Sec. S V for the *NVT* simulations details, and Sec. S VI for the *NPT* simulations details.

[126] Materials Cloud Archive, https://archive.materialscloud.org/record/2021.15.

[127] R. Car and M. Parrinello, Phys. Rev. Lett. **55**, 2471 (1985).

[128] P. Hohenberg and W. Kohn, Phys. Rev. **136**, B864 (1964).

[129] W. Kohn and L. J. Sham, Phys. Rev. **140**, A1133 (1965).

[130] M. C. Payne, M. P. Teter, D. C. Allan, T. Arias, and A. J. Joannopoulos, Rev. Mod. Phys. **64**, 1045 (1992).

[131] G. Galli and A. Pasquarello, in *Computer Simulation in Chemical Physics* (Springer, Dordrecht, 1993), pp. 261–313.

[132] P. Giannozzi, S. Baroni, N. Bonini, M. Calandra, R. Car, C. Cavazzoni, D. Ceresoli, G. L. Chiarotti, M. Cococcioni, I. Dabo *et al.*, J. Phys.: Condens. Matter **21**, 395502 (2009).

[133] D. K. Remler and P. A. Madden, Mol. Phys. **70**, 921 (1990).

[134] G. Pastore, E. Smargiassi, and F. Buda, Phys. Rev. A **44**, 6334 (1991).

[135] D. R. Hamann, Phys. Rev. B **88**, 085117 (2013).

[136] M. Schlipf and F. Gygi, Comput. Phys. Commun. **196**, 36 (2015).

[137] G. Prandini, A. Marrazzo, I. E. Castelli, N. Mounet, and N. Marzari, npj Comput. Mater. **4**, 72 (2018).

[138] K. Lejaeghere, G. Bihlmayer, T. Björkman, P. Blaha, S. Blügel, V. Blum, D. Caliste, I. E. Castelli, S. J. Clark, A. Dal Corso *et al.*, Science **351**, aad3000 (2016).

[139] K. F. Garrity, J. W. Bennett, K. M. Rabe, and D. Vanderbilt, Comput. Mater. Sci. **81**, 446 (2014).

[140] A. Dal Corso, Comput. Mater. Sci. **95**, 337 (2014).

[141] J. P. Perdew, K. Burke, and M. Ernzerhof, Phys. Rev. Lett. **77**, 3865 (1996).

[142] S. Nosé and M. Klein, Mol. Phys. **50**, 1055 (1983).

[143] G. J. Martyna, M. L. Klein, and M. Tuckerman, J. Chem. Phys. **97**, 2635 (1992).

[144] M. Parrinello and A. Rahman, Phys. Rev. Lett. **45**, 1196 (1980).

[145] M. Bernasconi, G. Chiarotti, P. Focher, S. Scandolo, E. Tosatti, and M. Parrinello, J. Phys. Chem. Solids **56**, 501 (1995).

[146] W. S. Price, Concepts Magn. Res.: Ed. J. **9**, 299 (1997).

[147] A. Einstein, Ann. Phys. **322**, 549 (1905).

[148] D. Chandler, *Introduction to Modern Statistical Mechanics* (Oxford University Press, Oxford, 1987).

[149] D. Frenkel and B. Smit, *Understanding Molecular Simulation: From Algorithms to Applications* (Elsevier, Amsterdam, 2001), Vol. 1.

[150] X. He, Y. Zhu, A. Epstein, and Y. Mo, npj Comput. Mater. **4**, 18 (2018).

[151] M. P. Allen and D. J. Tildesley, *Computer Simulation of Liquids* (Oxford University Press, Oxford, 2017).

[152] F. Grasselli and S. Baroni, Nat. Phys. **15**, 967 (2019).

[153] M. French, S. Hamel, and R. Redmer, Phys. Rev. Lett. **107**, 185901 (2011).

[154] K. R. Harris, J. Phys. Chem. B **114**, 9572 (2010).

[155] A. France-Lanord and J. C. Grossman, Phys. Rev. Lett. **122**, 136001 (2019).

[156] A. Afandak and H. Eslami, J. Phys. Chem. B **121**, 7699 (2017).

[157] R. Kubo, J. Phys. Soc. Jpn. **12**, 570 (1957).

[158] P. Atkins and J. De Paula, *Elements of Physical Chemistry* (Oxford University Press, Oxford, 2013).

[159] L. Kahle, A. Marcolongo, and N. Marzari, Phys. Rev. Mater. **2**, 065405 (2018).

[160] V. Tyuterev and N. Vast, Comput. Mater. Sci. **38**, 350 (2006).

[161] F. Murnaghan, Proc. Natl. Acad. Sci. USA **30**, 244 (1944).

[162] M.-J. Uddin and S.-J. Cho, Sustain. Energy Fuels **2**, 1458 (2018).

[163] G. Murch, Solid State Ion. **7**, 177 (1982).

[164] W. Donner, C. Chen, M. Liu, A. J. Jacobson, Y.-L. Lee, M. Gadre, and D. Morgan, Chem. Mater. **23**, 984 (2011).

[165] K. Kerman, A. Luntz, V. Viswanathan, Y.-M. Chiang, and Z. Chen, J. Electrochem. Soc. **164**, A1731 (2017).

[166] H. Muramatsu, A. Hayashi, T. Ohtomo, S. Hama, and M. Tatsumisago, Solid State Ion. **182**, 116 (2011).

[167] G. Zhao, K. Suzuki, T. Seki, X. Sun, M. Hirayama, and R. Kanno, J. Solid State Chem. **292**, 121651 (2020).

[168] S. Muy, J. C. Bachman, H.-H. Chang, L. Giordano, F. Maglia, S. Lupart, P. Lamp, W. G. Zeier, and Y. Shao-Horn, Chem. Mater. **30**, 5573 (2018).

[169] G. Zhao, K. Suzuki, M. Yonemura, M. Hirayama, and R. Kanno, ACS Appl. Energy Mater. **2**, 6608 (2019).

[170] Y. Sun, W. Yan, L. An, B. Wu, K. Zhong, and R. Yang, Solid State Ion. **301**, 59 (2017).

[171] W. Zhang, D. A. Weber, H. Weigand, T. Arlt, I. Manke, D. Schröder, R. Koerver, T. Leichtweiß, P. Hartmann, W. G. Zeier, and J. Janek, ACS Appl. Mater. Interfaces **9**, 17835 (2017).

[172] F. Du, X. Ren, J. Yang, J. Liu, and W. Zhang, J. Phys. Chem. C **118**, 10590 (2014).

[173] C. Hu, Z. Wang, Z. Sun, and C. Ouyang, Chem. Phys. Lett. **591**, 16 (2014).

[174] K. Fujimura, A. Seko, Y. Koyama, A. Kuwabara, I. Kishida, K. Shitara, C. A. Fisher, H. Moriwake, and I. Tanaka, Adv. Energy Mater. **3**, 980 (2013).

[175] L. Verlet, Phys. Rev. **159**, 98 (1967).

[176] M. Parrinello and A. Rahman, J. Appl. Phys. **52**, 7182 (1981).

[177] P. H. Hünenberger, in *Advanced Computer Simulation*, Advances in Polymer Science Vol. 173 (Springer, Berlin, Heidelberg, 2005), pp. 105–149.

[178] L. Kahle, A. Marcolongo, and N. Marzari, Energy Environ. Sci. **13**, 928 (2020).

[179] H. C. Andersen, J. Chem. Phys. **72**, 2384 (1980).

[180] K. Momma and F. Izumi, J. Appl. Crystallogr. **44**, 1272 (2011).